Optical properties of defects in nitride semiconductors

Ingo Tischer[a)]
Institute of Quantum Matter, Semiconductor Physics Group, University of Ulm, 89081 Ulm, Germany; and Richter lighting technologies GmbH, 73540 Heubach, Germany

Matthias Hocker and Benjamin Neuschl
Institute of Quantum Matter, Semiconductor Physics Group, University of Ulm, 89081 Ulm, Germany

Manfred Madel
Institute of Quantum Matter, Semiconductor Physics Group, University of Ulm, 89081 Ulm, Germany; and UMS GmbH, 89081 Ulm, Germany

Martin Feneberg
Institute of Quantum Matter, Semiconductor Physics Group, University of Ulm, 89081 Ulm, Germany; and Otto von Guericke University, 39106 Magdeburg, Germany

Martin Schirra
Institute of Quantum Matter, Semiconductor Physics Group, University of Ulm, 89081 Ulm, Germany; and Hochschule Kempten, 87435 Kempten, Germany

Manuel Frey
Institute of Quantum Matter, Semiconductor Physics Group, University of Ulm, 89081 Ulm, Germany; and U-L-M Photonics, 89081 Ulm, Germany

Manuel Knab and Pascal Maier
Institute of Quantum Matter, Semiconductor Physics Group, University of Ulm, 89081 Ulm, Germany

Thomas Wunderer
Institute of Optoelectronics, University of Ulm, 89081 Ulm, Germany; and Palo Alto Research Center, Palo Alto, California 94304, USA

Robert A.R. Leute
Institute of Optoelectronics, University of Ulm, 89081 Ulm, Germany; and Automotive Lighting, 72762 Reutlingen, Germany

Junjun Wang and Ferdinand Scholz
Institute of Optoelectronics, University of Ulm, 89081 Ulm, Germany

Johannes Biskupek, Jörg Bernhard, and Ute Kaiser
Electron Microscopy Group of Materials Science, University of Ulm, 89069 Ulm, Germany

Ulrich Simon
Scientific Computing Centre Ulm, University of Ulm, 89081 Ulm, Germany

Levin Dieterle
Institute of Electron Microscopy, Karlsruhe Institute of Technology, 76131 Karlsruhe, Germany; and VEGA Grieshaber KG, 77761 Schiltach, Germany

Heiko Groiss
Institute of Electron Microscopy, Karlsruhe Institute of Technology, 76131 Karlsruhe, Germany; and Institute of Semiconductor and Solid State Physics, Johannes Kepler University Linz, 4040 Linz, Austria

Erich Müller and Dagmar Gerthsen
Institute of Electron Microscopy, Karlsruhe Institute of Technology, 76131 Karlsruhe, Germany

Klaus Thonke
Institute of Quantum Matter, Semiconductor Physics Group, University of Ulm, 89081 Ulm, Germany

(Received 29 May 2015; accepted 18 August 2015)

Group III nitrides are promising materials for light emitting diodes (LEDs). The occurrence of structural defects strongly affects the efficiency of these LEDs. We investigate the optical properties of basal plane stacking faults (BFSs), and the assignment of specific spectral features to distinct defect types by direct correlation of localized emission bands measured by cathodoluminescence in

Contributing Editor: Joan M. Redwing
[a)]Address all correspondence to this author.
e-mail: ingo.tischer@alumni.uni-ulm.de
This paper has been selected as an Invited Feature Paper.
DOI: 10.1557/jmr.2015.273

 © Materials Research Society 2015

https://doi.org/10.1557/jmr.2015.273 Published online by Cambridge University Press

a scanning electron microscope with defects found in high resolution (scanning) transmission electron microscopy and electron beam induced current at identical sample spots. Thus, we are able to model the electronic structure of BSFs addressing I_1, I_2, and E type BSFs in GaN and AlGaN with low Al content. We find hints that BSFs in semipolar AlGaN layers cause local changes of the Al content, which strongly affects the usability of AlGaN as an electron blocking layer in nitride based LEDs.

I. INTRODUCTION

In times of increasing energy costs and more focus on environmental problems, the replacement of conventional incandescent lamps by light emitting diodes (LEDs) is a hot topic. White light from LEDs has to be generated by either the suitable phosphor for light conversion,[1,2] or by synthesis using red, blue, and green emitting LEDs. While growth of efficient blue LEDs based on the group III nitrides was achieved and rewarded with the Nobel Prize 2014, the green InGaN LEDs still suffer from efficiency problems.[3] This phenomenon is labeled as *green gap*. Another unsolved issue is the reduced efficiency for higher LED currents. The physical origin of this so-called *droop* is still under discussion.[4–10] The use of semipolar materials may be a promising approach.

However, the growth of the group III nitrides is usually performed on foreign substrates, resulting in dislocations, stacking faults (SFs), and strain due to the lattice mismatch to the substrate. SFs and dislocations are reported to reduce the device efficiency by providing alternative current paths for diodes,[11–13] transistors,[14–16] LEDs,[17] and for n-doped GaN layers as well.[18]

In this work, we focus on the electronic and corresponding optical properties of basal plane stacking faults (BSFs) in semipolar GaN and AlGaN structures. For these BSFs, a possible model for their electronic band structure in the group III nitrides is discussed. These calculations are compared with recent spectroscopic results. A detailed analysis of the energy shift for specific defect types allows to distinguish between shifts in emission energy caused by composition fluctuations for an AlGaN layer and the stacking fault related emission bands. This distinction yields information about local changes in Al content introduced by the BSFs themselves.

II. QUANTUM WELL (QW) MODEL FOR THE BSFS

The stacking sequence along the wurtzite GaN (0001) direction is given by $\ldots ABAB\ldots$,[19,20] where A and B denote hexagonal closed-packed GaN bilayers. The distance between two A or B planes is the c lattice constant. If this sequence is distorted resulting in the sequence $\ldots ABAB\underline{ABC}BCBC\ldots$ the I_1 type BSF is formed. The underlined part marks the defect itself. The I_2 type BSF is indicated by the stacking sequence $\ldots ABAB\underline{ABCA}CACA\ldots$. The typical arrow shape of the BSF of I_3 type looked at in the a plane is created by the sequence $\ldots ABAB\underline{ABCBA}BABA\ldots$. Finally, the extrinsic (E type) BSF $\ldots AB\underline{ABCA}BAB\ldots$ is formed by introducing an additional misplaced plane without any further change in stacking order.

In the sequence I_1, I_2, and E type BSF each of the defects shows a part of the stacking order $\ldots ABCABCABC\ldots$, which can be considered as an inclusion of zinkblende material along the cubic (111) direction. The thickness of these defects changes by one half of the c lattice constant from one to the other except for the I_3 BSF, which does not follow this rule, but might be regarded as a zinkblende layer.

The zinkblende lattice order leads to a common approach to model the electronic structure. The fundamental low temperature band gap of cubic GaN (3.302 eV from Ramírez-Flores et al.[21]) is smaller than the wurtzite one (3.504 eV from Monemar[22]). Several groups (i.e., Rebane et al.,[23] Albrecht et al.,[24] Bandić et al.[25]) proposed a type I QW model using the wurtzite material as a matrix to embed the cubic insertion. The transition from the QW ground state of the conduction band to the valence band results in a transition energy of 3.41 eV. This simple model works fine for the I_1 type defect, but fails for the other defects, since the increase in thickness necessary to explain the shift of the related emission bands, is too high.[26]

The basic model was supplemented by Sun et al.,[27] Skromme et al.,[28] and Liu et al.[29] These authors take into account the spontaneous polarization across the wurtzite/zinkblende GaN interface. The resulting electrical field tilts the band structure in the QW lowering the transition energy. Applying this model, the transition energy at the I_1 and the I_2 BSF could be calculated in rather good agreement. Still, a type I band alignment was assumed.

Lähnemann et al.[30,31] report about their different approach to model the electronic structure. They alternatively used a type I or a type II band alignment for calculations, which both yield transition energies compatible with the experimental results on GaN nanorods with high BSF densities, which did not allow for clear separation of I_1 and other types of BSFs. From the energy shift between the different defect types, the authors are able to calculate the spontaneous polarization of the GaN material applying a simple capacitor model.[31] Additionally, a possible coupling of the closely neighboring BSFs is reported to further decrease the emission energies in areas with high basal plane defect densities.[31]

https://doi.org/10.1557/jmr.2015.273 Published online by Cambridge University Press

Our model is a similar approach. The discontinuity in polarization at the interface between wurtzite and cubic material results in charges on the interface plane. Our model assumes an exponential decrease of the locally induced changes of the band energies in the QW barriers with the characteristic length being the (doping dependent) Debye length. For the calculations, an unintentional background doping level of $10^{17}/cm^{-3}$ was assumed,[32] resulting in a Debye length of 2.1 nm. The band offset is distributed in such a way, that 70% occur in the conduction band (upper red curve in Fig. 1), and 30% in the valence band (lower red curve), as suggested by Piprek and Nakamura.[33] The calculations were performed employing the matrix method of Van der Maelen Urìa et al.[34] assuming fully relaxed material. The model was calibrated using the transition energy of 3.41 eV for the I_1 BSF[29] which results in an *effective* thickness of the defect of 1.1 *c* lattice constants of wurtzite GaN.

The simulation results together with the experimental emission energies and references are summarized in Table I. The parameters used for the simulation are listed in Table II for the wurtzite, and in Table III for the cubic material, respectively.

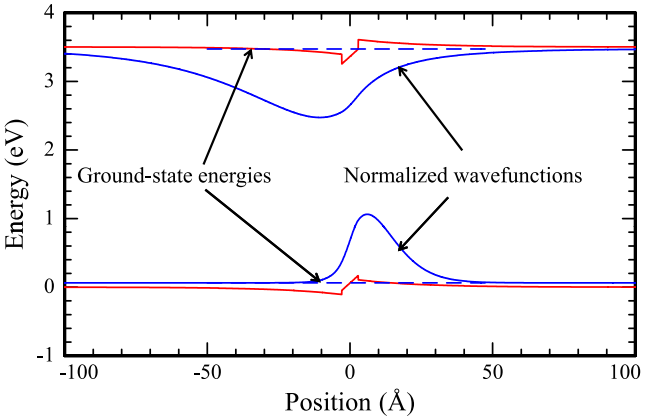


FIG. 1. Conduction band (upper red curve) and valence band (lower red curve) structure of I_1 BSF: ground state wave functions (solid blue) and energy (dashed blue).

TABLE I. Calculated emission energies and corresponding references. The experimental values are explained in the next sections. The yet unknown defect related bands (n.n.), presumably BSFs, were found experimentally (see below) and therefore added to the table.

BSF type	Thickness $\times c_{w-GaN}$	Energy (calc.) (eV)	Energy (exp.) (eV)	References
I_1	1.1	3.410	3.41	3.41 eV (Ref. 29)–3.43 eV (Ref. 35)
I_2	1.6	3.345	3.35	3.35 (Ref. 30), 3.3588 eV (Ref. 27)
E	2.1	3.274	3.26	3.30 eV (Ref. 30)
n.n.	2.6	3.199	3.19	...
n.n.	3.1	3.115	3.09	...

III. EXPERIMENTAL

A. Sample structure

All experimental results presented here were obtained from a similar type of samples, grown by metal organic vapor phase epitaxy. On a sapphire substrate first a *c* oriented GaN template was grown and a SiO_2 layer was evaporated subsequently. This cover was structured lithographically resulting in open stripes aligned along the GaN $[11\bar{2}0]$ direction with an opening of 3 μm and a period of 20 μm. On this masked substrate, selective area growth of GaN was performed using the lateral overgrowth mechanism to achieve semipolar side facets. This approach results in a reduced density of dislocations by bending them into horizontal direction.[50] The sample consists of stripes with naturally stable semipolar $\{10\bar{1}1\}$ side facets and a triangular cross section as sketched in Fig. 2. Details of the growth process can be found elsewhere.[50]

Three different samples were investigated. Sample No. 1 does not have any additional layers and no intentional doping. On sample No. 2, a thin layer of AlGaN with a nominal Al content of 5 and a thickness of approximately 200 nm was deposited. Sample No. 3 is a full LED structure, for which the GaN stripe buffer is n-doped. A 3-fold InGaN/GaN QW, an AlGaN electron blocking layer (EBL), and a final p-doped GaN layer were grown on the side facets. On both the p- and the n-side ohmic contacts were created and wire bonded.

TABLE II. Material parameters for wurtzite GaN and AlN. Electron mass is referenced as m_0.

	GaN	AlN
a lattice constant	3.189 Å (Ref. 36)	3.112 Å (Ref. 37)
c lattice constant	5.185 Å (Ref. 36)	4.982 Å (Ref. 37)
Fundamental bandgap	3.503 eV (Ref. 22)	6.23 eV (Ref. 38)
Spont. polarization	−0.029 C/m^2 (Ref. 39)	−0.090 C/m^2 (Ref. 38)
Effective electron mass	$0.22m_0$ (Ref. 40)	$0.32m_0$ (Ref. 41)
Effective hole mass	$2.2m_0$ (Ref. 42)	$3.31m_0$ (Ref. 41)
Dielectric constant $\varepsilon_{\parallel}$	10.1 (Ref. 43)	9.21 (Ref. 44)
Dielectric constant $\varepsilon_{\perp}$	9.28 (Ref. 43)	7.65 (Ref. 44)
Donor density	10^{17} cm^{-3} (Ref. 32)	10^{17} cm^{-3} (Ref. 32)
Bowing parameter	...	0.85 eV (Ref. 45)

TABLE III. Material constants for cubic GaN and AlN. Electron mass is referenced as m_0.

	GaN	AlN
Fundamental bandgap (eV)	3.302 (Ref. 46)	5.3 (Ref. 47)
Effective electron mass	$0.19m_0$ (Ref. 46)	$0.3m_0$ (Ref. 41)
Effective hole mass	$1.95m_0$ (Ref. 41)	$3.98m_0$ (Ref. 41)
Dielectric constant ε	9.7 (Ref. 48)	8.07 (Ref. 47)
Bowing parameter	...	1.1 eV (Ref. 49)

https://doi.org/10.1557/jmr.2015.273 Published online by Cambridge University Press

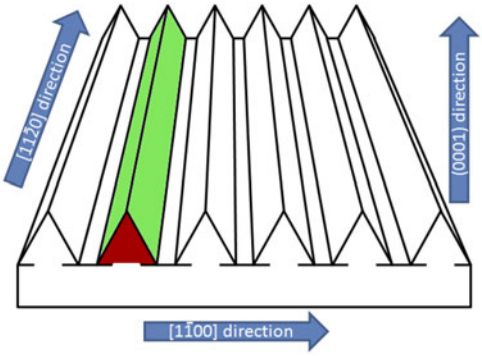


FIG. 2. Sketch of sample structure. Between the stripes, the SiO_2 mask is visible. The crystal directions are indicated by the arrows. The (green) side facets are $\{10\bar{1}1\}$ planes, the cross sections (red) are $\{11\bar{2}0\}$ planes.

For optical investigation, the samples were cleaved mechanically to get access to the stripes' cross sections.

B. Experimental setups

All cathodoluminescence (CL) investigations were performed in a LEO DSM 982 scanning electron microscope (SEM; Carl Zeiss AG, Oberkochen, Germany) equipped with a 100 μm thin diameter ultraviolet enhanced glass fiber for light collection. The fiber tip is placed on the sample surface close to the region of interest without negatively influencing the SEM picture quality. The collected light can be led to several detection systems. For recording highly resolved spectra, a liquid nitrogen cooled charge coupled device camera connected to a 90 cm focal length monochromator is used. Alternatively, the luminescence intensity can be detected with a photomultiplier tube and recorded simultaneously with the SEM micrographs for a direct correlation between the excitation spot and the CL intensity. These maps can be recorded either panchromatic or spectrally resolved using a 25 cm focal length monochromator. The sample is mounted on the cold finger of a helium cooled cryostat. This allows to cover the temperature range between 4 and 475 K.

The same SEM setup can be equipped with a detection system for electron beam induced current (EBIC). The current amplifier is installed inside the SEM chamber to avoid signal distortion from the environment. The signal cables can be kept short resulting in very low parasitic capacitance of the device. Together with surface mounted devices and a small form factor printed circuit board a reliable signal to noise ratio is achieved. The amplified EBIC signal is again recorded simultaneously with the SEM detector signal, which allows to spatially correlate the EBIC signal. Low temperature combined spatially correlated EBIC and CL measurements are discussed elsewhere.[51]

The transmission electron microscopy (TEM) investigations were performed using two different TEM types. A Philips CM 20 TEM (Koninklijke Philips N.V., Eindhoven, The Netherlands) was used to investigate the LED sample. The other two samples were characterized with aberration corrected FEI Titan[3] TEMs in scanning mode [scanning transmission electron microscopy (STEM)] (FEI, Eindhoven, The Netherlands). All TEM lamella preparations were done by focused ion beam (FIB), with a protective platinum layer evaporated on the sample top surface to prevent the area of interest to be etched. These FIB cuts were performed at those sample areas, where CL investigations were completed before. This allows a direct correlation of spectral (from CL), electrical (partly from EBIC), and structural (from TEM) properties.

For high resolution X-ray diffraction (XRD) measurement, a Bruker D8 system (Bruker Corporation, Billerica, Massachusetts) was used. Reciprocal space maps of asymmetric $(11\bar{2}4)$ and $(1\bar{1}06)$ reflexes were recorded. Thus, changes in lattice parameters can be investigated separately for directions parallel and perpendicular to the stripes.

C. BSF in semipolar GaN

Figure 3(b) shows the spectrum recorded on the triangular cross section of sample No. 1 (see SEM micrograph). The blue markers denote the spectral ranges, over which the maps were recorded. The spatial distributions (Figure 3(a)) of the selected wave length ranges differ strongly. Therefore, none of the peaks are just phonon replica of others.

The band at 3.41 eV is assigned to the BSF, I_1,[29] since it is aligned perpendicular to the (0001) direction. All other defect related contributions are localized close to the side facet surface, and no contributions from inner parts of the stripe can be detected. This allows to perform a measurement on a side facet to increase the spatial resolution and to clarify the extension of the defects. Figure 4(a) shows the exemplary CL intensity map of the emission around 3.33 eV. The band which shows a dot like pattern on the cross section continues on the side facet as a series of horizontal lines. The same behavior can be observed for all other contributions (not shown here, details see elsewhere[52]).

The exact defect type was determined by TEM. A thin lamella was cut out of the stripe region where the side facet investigations were performed at. The cut was made perpendicularly to the stripe allowing high resolution STEM on the very same area. The positions of all BSFs in this region were recorded [black crosses in Fig. 4(c)]. For comparison with the CL data, we used a Gaussian shape line with a full width at half maximum (FWHM) of 175 nm at each BSF position to model the diameter of the electron beam excitation volume, and to account for the exciton diffusion. Summing up these Gaussians as a function of the distance of the defects from the bottom corner of the structure, a TEM based BSF profile [blue upper curve in Fig. 4(c)] can be plotted and compared to CL profiles of the different defect bands. The profile for the 3.32 eV band is plotted in red (bottom curve). This CL profile can be obtained from the maps [see white

https://doi.org/10.1557/jmr.2015.273 Published online by Cambridge University Press

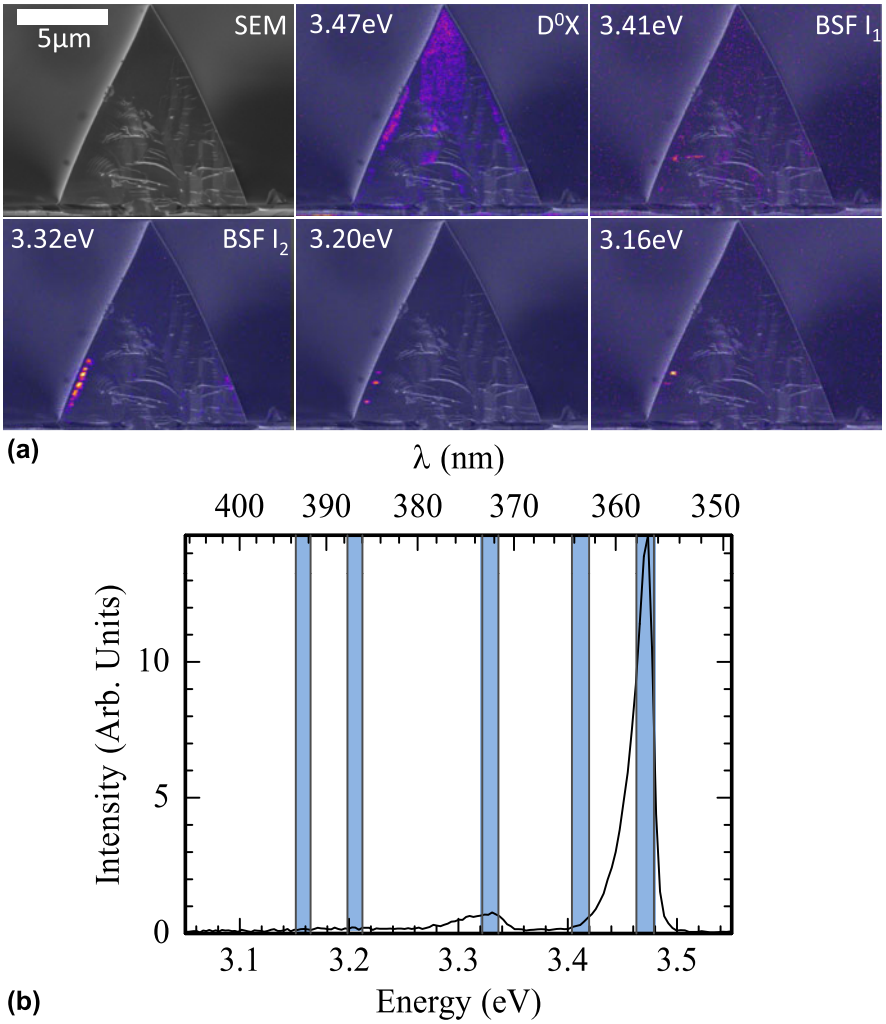


FIG. 3. (a) CL intensity maps as overlay on the corresponding SEM micrograph. Donor bound exciton of relaxed GaN at 3.47 eV, BSF I_1 at 3.41 eV,[29] BSF I_2 at 3.32 eV,[26,52] and two other strongly localized defect related bands at 3.20 and 3.16 eV. SEM electron energy 2 keV, temperature 10 K. (b) In the integral spectrum, the spectral range of each map is marked in blue color (2 keV primary electron energy, temperature 10 K).

rectangle in Fig. 4(a)]. Slightly below a distance of 4 µm from the bottom edge (see mark by double arrow), two isolated BFSs with an emission band at 3.33 eV can be observed. The slight shift as compared to the position found in the cross section is caused by a modified strain situation after mechanical sample cleaving. The high resolution STEM micrograph in Figure 4(b) shows one of these BSFs exemplarily. Both defects exhibit the stacking sequence characteristic for the I_2 type BSF as marked by colored dots. By virtue of this direct correlation, the emission band at 3.33 eV can be assigned unambiguously to the I_2 BSF.[26]

As mentioned above, several papers report this defect to cause the emission around 3.35 eV, which contradicts our findings. Within the QW model for the BSF, energy shifts due to strain have to be taken into account. We developed a model of the strain situation of the GaN stripe applying a 2D plane stress finite element (FE) simulation assuming linear elastic anisotropic material. Biaxial compressive strain in the substrate below was found in earlier CL investigations (not shown here). In our FE model, this strain was applied to the base of the stripe inside the mask opening. The result is plotted in Fig. 5. A thin layer with normal tensile strain in both the $(1\bar{1}00)$ and the (0001) direction is found on the sample surface in the bottom third of the side facet.

CL spectra from this area show an emission from donor bound excitons (D^0X) shifted from the relaxed value of 3.47 eV down by 30 meV to 3.44 eV. If we add this shift to the 3.32 eV emission energy we found for the I_2 BSF, we end up at an energy of 3.35 eV. This value is in accordance with our model calculation, and is also in good agreement with the values reported in literature.[27,30,31] Experimental values given in Table I were all corrected (added 30 meV) according to the strain situation determined from the spectral position of the shifted donor bound exciton band at the same sample position.

https://doi.org/10.1557/jmr.2015.273 Published online by Cambridge University Press

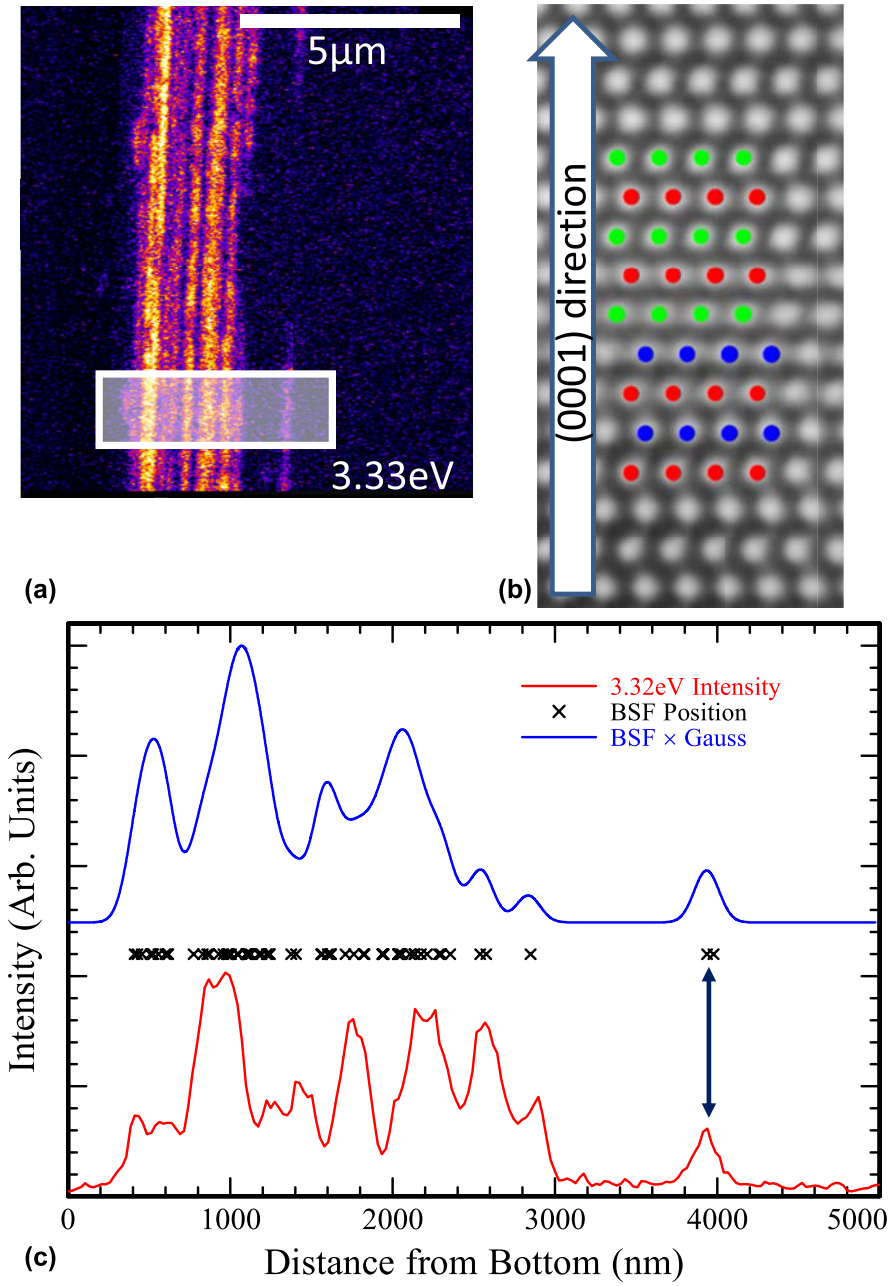


FIG. 4. (a) CL intensity map of the side facet at 3.33 eV. (b) Exemplary high resolution STEM micrograph of one of the two isolated defects at the position marked by the black double arrow. (c) Comparison of CL intensity profile taken from the positions marked by the white rectangle (red, lower curve) with the artificially broadened BSF positions (black crosses) created from the TEM micrographs (blue, upper curve) (2 keV primary electron energy, temperature 10 K).

D. BSF in semipolar AlGaN with low Al content

The results presented above are now applied to an AlGaN layer deposited on the GaN stripes' side facets (sample No. 2).[53] Here, the CL data analysis is more difficult, since a lower energy emission can be caused by defects, by strain, by lower aluminum content, or by any combination of these. Therefore, the absolute spectral position of the possible defect related emission does not provide sufficient information. Instead, the energy shift relative to the emission band from donor bound excitons yields the required details, since the D^0X emission energy is governed by the strain as well as by the aluminum content. The anisotropic strain behavior visible in the FE simulations (see Fig. 5) was confirmed experimentally by XRD investigations for both the GaN buffer and the AlGaN layer as shown in Fig. 6. Although the XRD signal was recorded averaging over a big number of stripes, the reflexes represent the different lattice constants

https://doi.org/10.1557/jmr.2015.273 Published online by Cambridge University Press

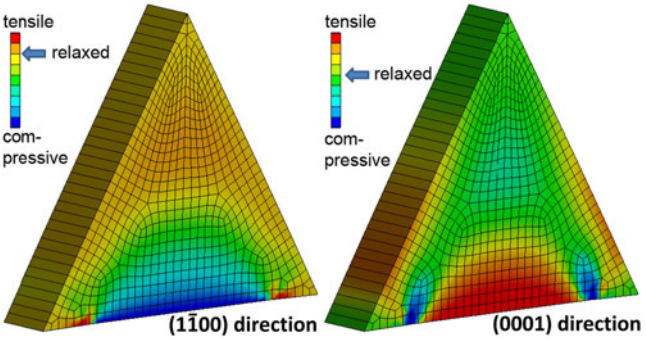


FIG. 5. Simulated normal strain on the cross section and surface of the GaN stripe grown by selective epitaxy over a mask opening. For the substrate, a biaxial compressive strain is known from earlier investigations (not shown here). This planar strain is applied through the mask opening to the stripe (strain contrasts at the bottom). A thin layer with tensile strain can be observed in the bottom third of the side facet.

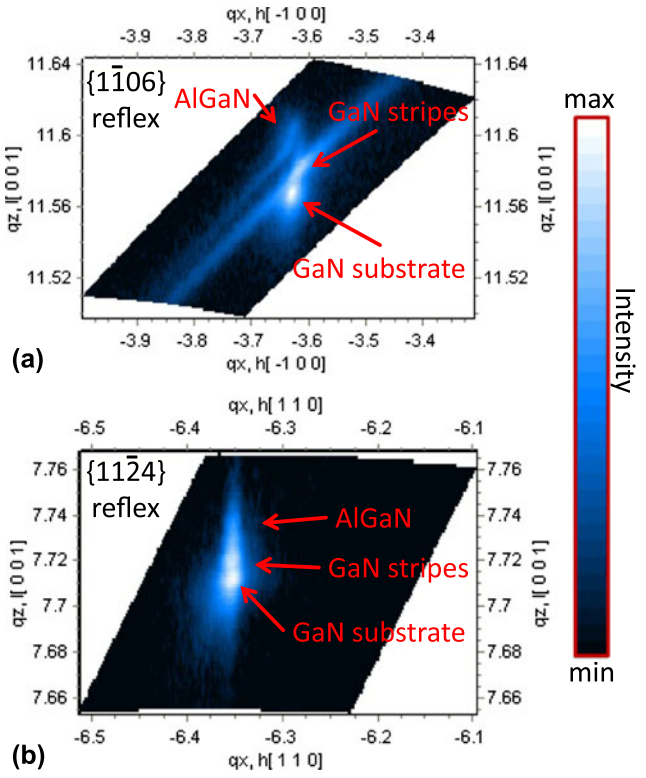


FIG. 6. XRD reciprocal space maps of the {1$\bar{1}$06} (a) and the {11$\bar{2}$4} (b) reflexes. The vertical axis is the reciprocal (0001) direction. The horizontal axes represent the reciprocal lattice constants perpendicular (a) and parallel (b) to the (11$\bar{2}$0) direction along the stripes. Along the stripes, the *a* lattice constant is matched for the different layers, which is not the case perpendicular to the stripe direction, where the *m* lattice constant changes.

of the biaxial compressively strained substrate material, the GaN stripes, and the AlGaN layer, respectively. The local variation inside each layer results in a broadening of the corresponding XRD peak. The lattice constant of the AlGaN layer should be smaller than the GaN layer constant due to the Al incorporation. Thus, different regions and layers can be assigned to their corresponding signals in the XRD graphs despite the averaging over several stripes. These graphs show that the lattice constant perpendicular to the (11$\bar{2}$0) stripe direction [i.e., along the *m* direction, see Fig. 6(a)] differs from the respective values for the substrate increasingly from the buffer to the topmost AlGaN layer, whereas the lattice constant parallel to the stripe [i.e., a direction, see Fig. 6(b)] remains unchanged. These findings are in full agreement with the averaged values found in the FE strain calculations. The XRD setup used does not resolve local changes along the vertical direction. Thus, the absolute values on the axes in Fig. 6 cannot be used as strain input in the model calculations for the BSF QW model.

For identification of SFs in the AlGaN layer, a similar approach as described above was chosen. The SEM-CL investigations on the AlGaN were performed at the very same stripe both in cross section and side facet view. Instead of addressing just the positions of the prominent peaks in the spectra, series of monochromatic CL maps within the spectral region of interest were recorded. The SEM micrographs were stored simultaneously allowing to spatially correlate the recorded CL maps accordingly to correct any shifts in SEM operation. This is necessary because of broad emission band containing the superimposed defect related CL contributions in the low energy tail. Thus, most of the defects do not provide a prominent peak position to record a CL map at. The corresponding TEM lamella again was prepared from the back side of the cross section to allow a perfect correlation of spatial distribution of the luminescence bands with their structural counterpart.

Figure 7(c) shows the integral spectrum recorded from the cross section of a single stripe of sample No. 2 as shown in the SEM micrograph. Several relatively broad contributions above the GaN fundamental band gap of 3.504 eV at low temperature are visible.[22] Figure 7(b) shows the color coded emission energy distribution. All luminescence comes from the top AlGaN layer only, while the GaN buffer below does not contribute. As known from energy dispersive X-ray (EDX) measurements (not shown here), the AlGaN layer thickness corresponds exactly to the region where the CL signal emerges.

The luminescence shows a clear blue shift from bottom to top as indicated by the thick arrow in the map in Fig. 7(b). This is caused by the three-dimensional growth mode, where the precursors are offered from top. Aluminum has a smaller surface diffusion length and arrives with higher concentration from the gas phase at the ridge, while the more mobile gallium evaporates at the edges. This results in a higher incorporation rate of Al close to the tip.[54]

In the lower half, some strongly pronounced spots with a lower emission-energy as the surrounding AlGaN matrix are visible (white arrows). This dot-like pattern

https://doi.org/10.1557/jmr.2015.273 Published online by Cambridge University Press

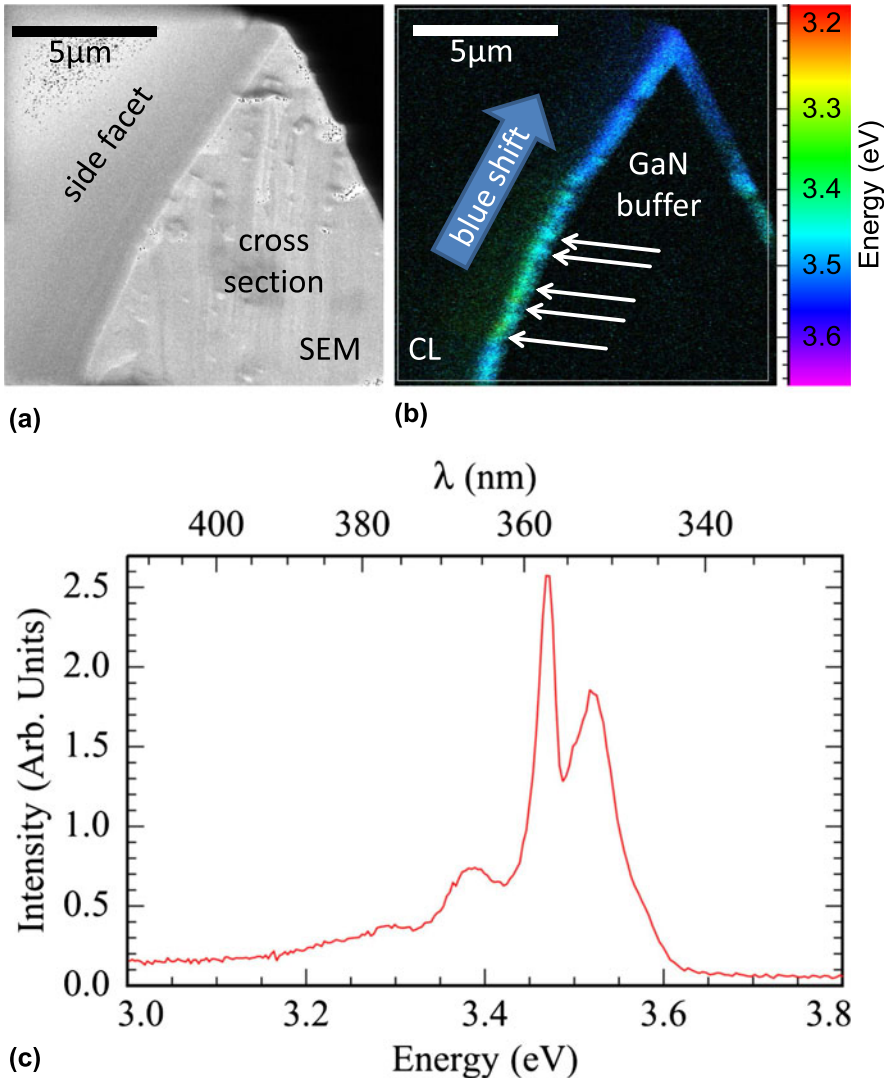


FIG. 7. SEM micrograph (a) and color coded emission energy map (b) of a cross section. The luminescence is created in the AlGaN layer only, while the GaN buffer does not contribute. The emission shows a blue shift from bottom to top. In the bottom half, localized defects with lower emission energies as compared to the AlGaN matrix are clearly resolved (white arrows). (c) CL spectrum from the integral cross section area of sample No. 2 shown in SEM micrograph (5 keV primary electron energy, temperature 10 K).

is the first indication for defects. Since luminescence is emitted by the AlGaN layer only while the GaN buffer remains dark, the AlGaN layer emission can be investigated by exciting it directly without being perturbed by luminescence from the buffer.

Figure 8(a) shows the SEM micrograph of the bottom part of the side facet, and Figure 8(b) is the corresponding energy color coded luminescence distribution map. Again, a stripe pattern similar to the one described above for the pure GaN material can be observed. Obviously, this pattern is caused by SFs in AlGaN.

The main problem for a clear assignment of the CL bands to a specific defect type is the inhomogeneous Al content. The energy shift between the defect itself and the emission from donor bound excitons in the surrounding defect-free material alone does not allow a clear assignment. We applied here the same approach as for pure GaN: from the backside of the cross section a lamella for TEM investigation was prepared by FIB. Again, the distribution of BSF was determined in the TEM micrograph, and a Gaussian (FWHM 175 nm) was applied to the histogram of BSF positions. The resulting TEM BSF profile in Fig. 8(c) (blue curve) allows to compare the CL and the defect distributions as a function of their distance from the bottom.

The black curve (3.50 eV) shows the emission from the donor bound excitons of high quality AlGaN with an Al content of approximately 2%. At the defect at around 1.5 µm distance from the bottom, there is a clear anticorrelation of the donor-related signal to the defect position marked by the two black arrows. At the same sample area, the emission band at 3.42 eV (red curve)

https://doi.org/10.1557/jmr.2015.273 Published online by Cambridge University Press

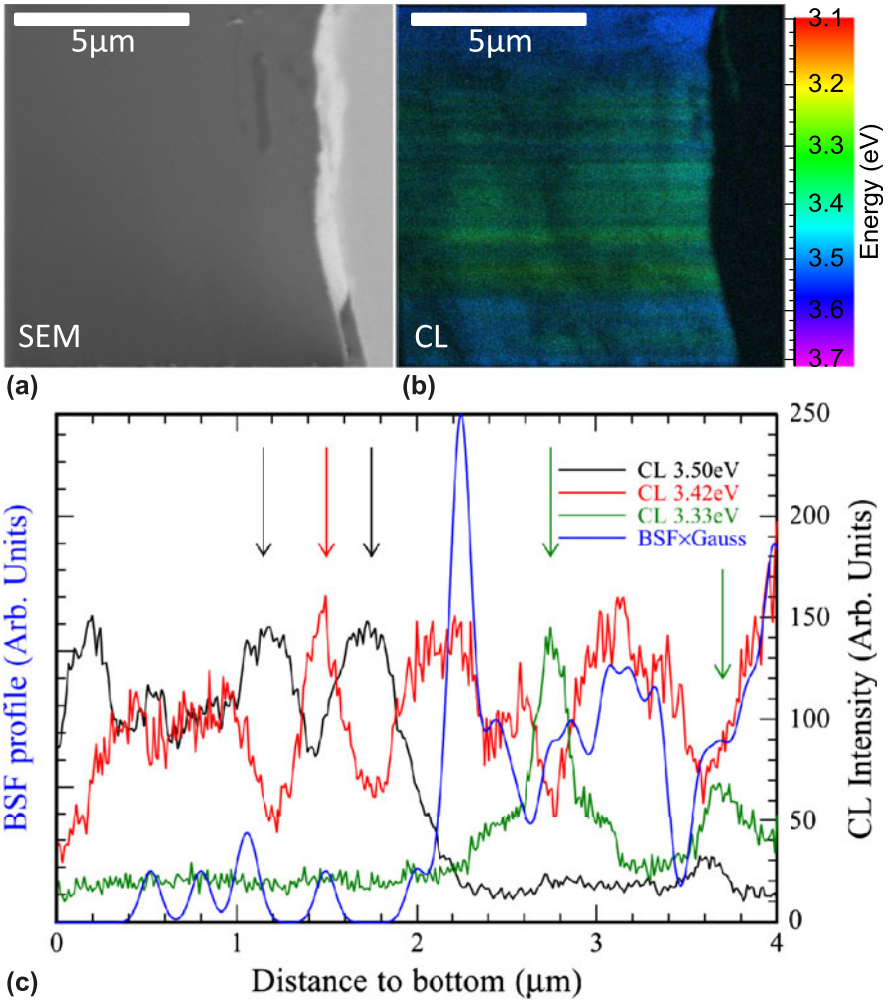


FIG. 8. SEM micrograph (a) and color coded emission energy map (b) of lower half of the side facet. The cross section on Fig. 7 can be seen on the right corner of the SEM micrograph. The emission distribution shows a line pattern with clearly red shifted horizontally aligned stripes surrounded by a more homogeneous matrix. (c) Comparison of the intensity profiles of the donor bound exciton band at 3.50 eV (black), the defect bands at 3.42 eV (red) and 3.33 eV (green) with the TEM BSF profile (blue). These profiles were created by averaging horizontally (5 keV primary electron energy, temperature 10 K).

shows clear positive correlation with the defect (red arrow), so that the latter band can be clearly assigned to this isolated BSF. The type of this BSF was determined again by high resolution STEM. Figure 9 shows the STEM micrograph, from which we determine the stacking sequence characteristic for the I_1 type BSF. Its emission is in this case red shifted by 80 meV relatively to the donor bound exciton emission energy of the surrounding AlGaN material.

A similar analysis can be done in principle for the band at 3.33 eV. But due to the high density of defects, no clear correlation to TEM results could be established in this case. However, the emission has to be BSF related, since no other defects besides dislocations and BSFs were found in TEM. Assuming the same Al content of the high quality AlGaN in the direct vicinity as used for the I_1 type BSF before, an energy shift of 170 meV from the AlGaN donor bound exciton emission energy can be calculated for the 3.33 eV band.

These two defect bands again can be compared to simulation results, calculated with the QW model described above for the BSFs. Vegard's law[55] was used to interpolate the lattice parameters etc. for AlGaN from the constants for pure GaN and pure AlN. For the fundamental band gap, the bowing parameter $b = 0.85$ eV[45] was used. This approximation is valid since the Γ_9 valence band is the topmost valence band for these low aluminum concentrations.[45] The QW model was calibrated with the defect at 3.42 eV for the given Al content, assuming fully relaxed material without any strain. This results in a nominal active thickness of the I_1 type BSF of 1.2 lattice constants of wurtzite AlGaN. Table IV summarizes the calculated and the experimental results.

https://doi.org/10.1557/jmr.2015.273 Published online by Cambridge University Press

The calculated and the measured values for the presumable I_2 type BSF differ by 20 meV. A possible explanation for this behavior could be a reduced Al content inside the cubic BSF insertion. This results in a deeper well and therefore in a larger red shift. Unfortunately, this could not be confirmed by TEM-EDX due to the very low Al content close to or below the detection limit. However, if this explanation is taken into consideration, a big impact of BSF on the homogeneity of the Al content in semipolar AlGaN layers is expected. Some more details about this investigation can be found elsewhere.[53]

E. Defects in a semipolar AlGaN EBL

The EBL of an LED structure is used to confine the charge carriers inside the active region, where the QWs are localized. For a detailed investigation of the optical and structural properties of defects inside a semipolar LED structure, sample No. 3, taken from a very early stage of optimization, was selected. This sample shows a relatively high leakage current in *I(V)* measurements (not shown here), and it exhibits a low electroluminescence efficiency.

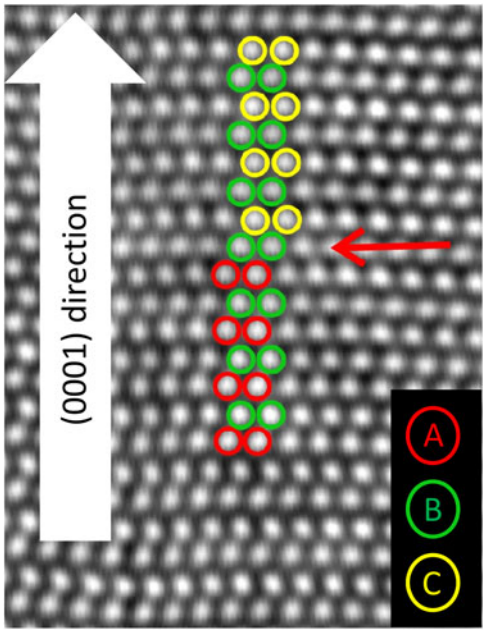


FIG. 9. High resolution STEM micrograph of the defect at 1.5 μm. The colored letters indicate the stacking sequence, the red arrow the I_1 type BSF itself.

On the same sample region, both spatially resolved panchromatic SEM-CL and SEM-EBIC measurements were performed. The results are presented in Fig. 10. The CL and EBIC maps are strongly inhomogeneous. But there are only few spots (red and green circles in Fig. 10) with direct (anti) correlation of CL and EBIC distributions.

The CL emission is dominated by the QWs. If the CL signal at some spot is weaker than at the surrounding material, the QWs might be defective. If the EBIC signal is less intense as well, it can be concluded that defects in this area affect both the wells and the pn junction. In this case, a defect penetrating through the whole structure is expected.

If the CL signal is weaker, but the EBIC signal remains the same, then just the QWs suffer from defects and vice versa.

The most interesting observation is that there are localized spots, where the EBIC signal is stronger than in the surrounding material. It makes no sense to assume an even better pn junction, but instead it seems to be easier for the current to reach the contacts. Since the CL signal at these spots does not show any specific changes, changes of the QW properties can be ruled out as reason. Thus, the EBL is the only remaining part which can cause this phenomenon.

To check this idea, TEM investigations of the EBL were carried out on a lamella prepared by FIB. Figure 11 (a) shows a TEM micrograph of the EBL and the topmost QW (light green arrow). The light gray contrast shows the presence of AlGaN. At the position denoted by the red arrow, the EBL is interrupted, and a much lower Al content is found. In TEM, many of these defect structures were found. Figure 11(b) is one of those structures in higher magnification. The red dashed lines indicate the position of the AlGaN EBL. There are two distinct structures, denoted by the blue and the yellow rectangle. The stacking sequence inside the blue one is clearly hexagonal, while inside the yellow one, the aligned diagonal structures merely look cubic. For clarification, the local fast Fourier transform pattern (FFT) of these two areas was recorded and compared with simulations for zincblende and wurtzite material. The results are shown in Fig. 12. The upper row contains the calculated patterns, the lower row shows the experimental ones. The left column is the cubic material; the hexagonal one is on the right. It can be seen clearly, that the calculation

TABLE IV. Calculated emission energies and corresponding experimental values. c_{AlGaN} is the calculated c lattice constant of AlGaN for the given Al content of 2%.

Emission type	Thickness × c_{AlGaN}	Energy (calc.) (eV)	Shift (calc.) (eV)	Energy (exp.) (eV)	Shift (exp.) (eV)
D^0X	...	3.50	...	3.50	...
I_1	1.2	3.42	0.08	3.42	0.08
I_2	1.7	3.35	0.15	3.33	0.17

https://doi.org/10.1557/jmr.2015.273 Published online by Cambridge University Press

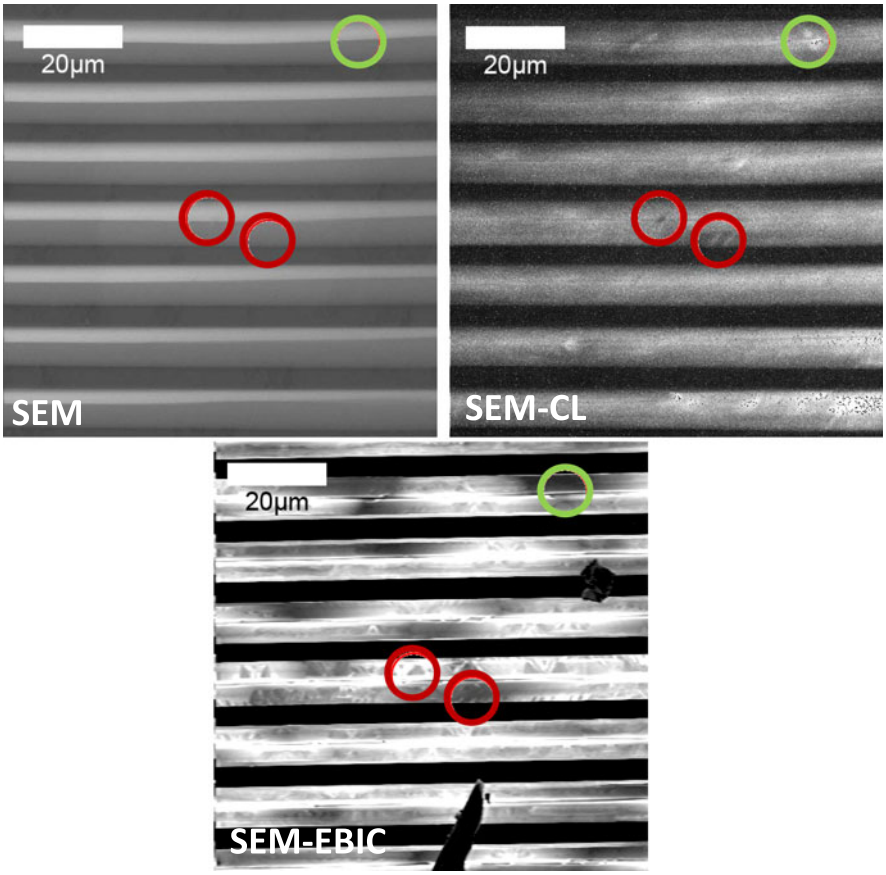


FIG. 10. Topview SEM, panchromatic SEM-CL, and SEM-EBIC micrographs of the LED sample No. 3. The red circles mark points of interest, where inhomogeneities are visible in both CL and EBIC distributions. The green circle indicates an anticorrelation of EBIC and CL signal at the stripe top (9 keV primary electron energy at room temperature).

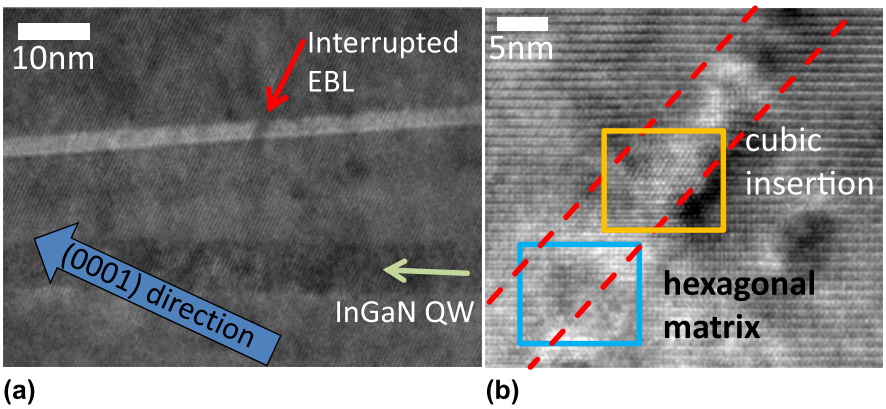


FIG. 11. (a) TEM micrograph of the interrupted EBL (red arrow) and the topmost InGaN QW (light green arrow). (b) High resolution TEM picture of a cubic insertion (yellow rectangle) in a wurtzite matrix, causing the EBL to be interrupted by a modified Al content. The red dashed lines show the EBL position.

and measurement coincide well. The main differences between cubic and hexagonal pattern are marked by the red circles. Moreover, that the reflex found inside the circles for the hexagonal material vanishes for the cubic confirming the existence of a cubic insertion inside the wurtzite matrix.

In the direct vicinity of this cubic insertion, the Al content is altered strongly, resulting in the interrupted EBL mentioned already. Thus, the higher leakage currents can be explained by a defective, interrupted semipolar EBL. The bad electroluminescence performance of this LED structure is caused by a combination of the

https://doi.org/10.1557/jmr.2015.273 Published online by Cambridge University Press

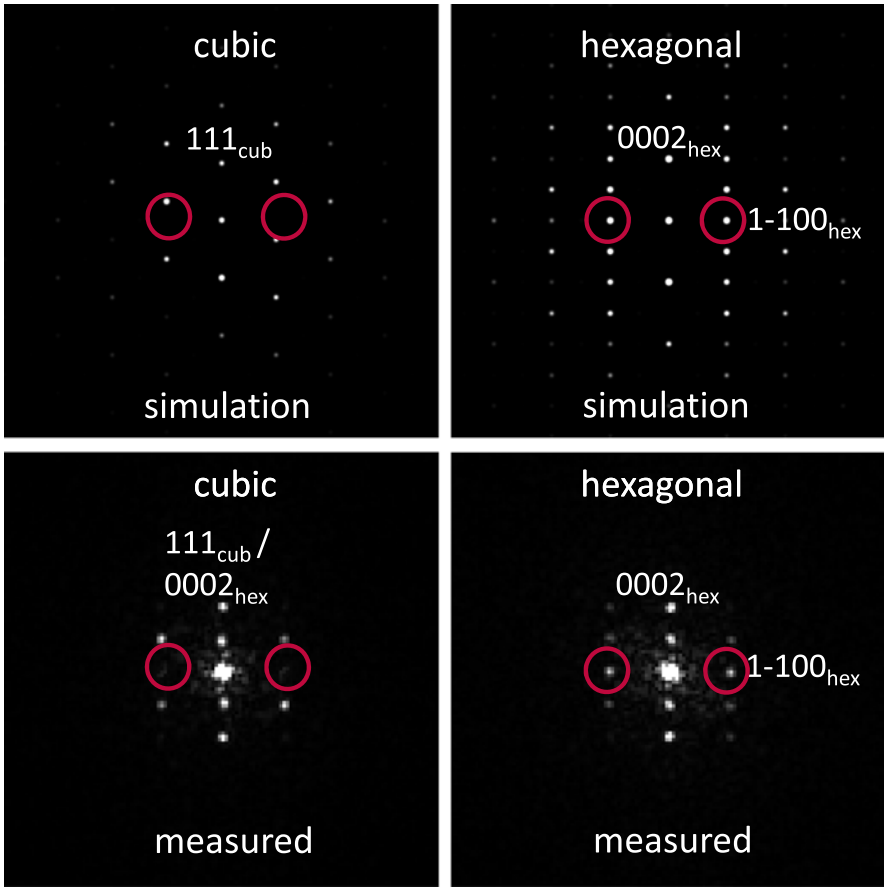


FIG. 12. Simulated (top row) and measured (bottom row) local FFT pattern of cubic (left column) and hexagonal (right column) AlGaN calculated from the high resolution TEM micrograph [Fig. 11(b)] from the regions highlighted by colored rectangles. The $\{1\bar{1}00\}$ reflex is absent in the cubic case.

reduced charge carrier confinement due to the interrupted EBL and of defective parts of the QW structure, where the QW material quality is worse.

IV. SUMMARY AND CONCLUSIONS

In this paper, we present a modified standard model describing the optical properties of BSF as cubic QWs embedded in a wurtzite matrix. In principle, this model can be extended to include the influence of strain. But although we found evidence for an anisotropic strain behavior of the GaN structure created by selective area growth, we cannot provide absolute values for the actual strain from the spectroscopic data. With this model it is possible to calculate the emission energies from different types of BSFs and to confirm these values with a combination of highly spatially and spectrally resolved SEM-CL investigations together with high resolution TEM images, recorded at the same sample region. This combination allows to unambiguously assign the band red shifted by 120 meV from its corresponding donor bound exciton to a I_2 type BSF. Some other emission bands can be tentatively assigned to BSFs with thicker cubic layers.

Applying the same model to a semipolar AlGaN layer with low Al content, we could assign an emission band red shifted by 80 meV from the surrounding emission of donor bound excitons to I_1 type BSF. This was proven experimentally using the same technique as described above. For the tentatively assigned I_2 type BSF we found an emission energy less red shifted than expected. This finding can be explained by a lower Al content in the cubic material resulting in a deeper QW. We ascribe the modification of the Al content to the presence of the BSFs.

Evidence for this assumption was also found in combined SEM-CL, SEM-EBIC, and TEM investigations of a semipolar LED structure with an EBL close to the InGaN/GaN QWs. Interruptions of the EBL with extremely low Al content were found close to cubic insertions. From this result, a possible negative influence of the BSFs and any other cubic insertion on the homogeneity of the Al content in semipolar wurtzite AlGaN layers can be concluded. This result has a strong impact on any structures, where AlGaN layers are used to confine charge carriers.

https://doi.org/10.1557/jmr.2015.273 Published online by Cambridge University Press

ACKNOWLEDGMENTS

The author thanks A. Eifert, G. Neusser, and C. Kranz from FIB Center at University of Ulm for their supporting SEM-EDX/FIB investigations. Parts of this work have been financially supported by the Deutsche Forschungsgemeinschaft within the transregional research group "PolarCoN". Further financial support by the German Federal Ministry of Education and Research (BMBF) within the framework of the "Deep UV-LED" project is gratefully acknowledged. Parts of this work received funding from the European Union's Seventh Framework Program within the research project "ALIGHT". H.G. acknowledges funding by the Austrian Science Fund (FWF): J3317-N27.

REFERENCES

1. P. Schlotter, R. Schmidt, and J. Schneider: Luminescence conversion of blue light emitting diode. *Appl. Phys. A* **64**, 417 (1997).
2. M. Raukas, J. Kelso, Y. Zheng, K. Bergenek, D. Eisert, A. Linkov, and F. Jermann: Ceramic Phosphors for Light Conversion in LEDs. *ECS J. Solid State Sci. Technol.* **2**, R3168 (2013).
3. S. Nakamura, M. Senoh, N. Iwasa, and S. Nagahama: High-Brightness InGaN Blue, Green and Yellow Light-Emitting Diodes with Quantum Well Structures. *Jpn. J. Appl. Phys.* **34**, L797 (1995).
4. M-H. Kim, M.F. Schubert, Q. Dai, J.K. Kim, E.F. Schubert, J. Piprek, and Y. Park: Origin of efficiency droop in GaN-based light-emitting diodes. *Appl. Phys. Lett.* **91**, 183507 (2007).
5. Y.C. Shen, G.O. Mueller, S. Watanabe, N.F. Gardner, A. Munkholm, and M.R. Krames: Auger recombination in InGaN measured by photoluminescence. *Appl. Phys. Lett.* **91**, 141101 (2007).
6. J. Piprek: Efficiency droop in nitride-based light-emitting diodes. *Phys. Status Solidi A* **207**, 2217 (2010).
7. J. Iveland, L. Martinelli, J. Peretti, J.S. Speck, and C. Weisbuch: Direct Measurement of Auger Electrons Emitted from a Semiconductor Light-Emitting Diode under Electrical Injection: Identification of the Dominant Mechanism for Efficiency Droop. *Phys. Rev. Lett.* **110**, 177406 (2013).
8. J. Piprek and Z.M. Simon Li: Origin of InGaN light-emitting diode efficiency improvements using chirped AlGaN multi-quantum barriers. *Appl. Phys. Lett.* **102**, 023510 (2013).
9. M. Binder, A. Nirschl, R. Zeisel, T. Hager, H-J. Lugauer, M. Sabathil, D. Bougeard, J. Wagner, and B. Galler: Identification of nnp and npp Auger recombination as significant contributor to the efficiency droop in (GaIn)N quantum wells by visualization of hot carriers in photoluminescence. *Appl. Phys. Lett.* **103**, 071108 (2013).
10. F. Bertazzi, M. Goano, X. Zhou, M. Calciati, G. Ghione, M. Matsubara, and E. Bellotti: Looking for Auger signatures in III-nitride light emitters: A full-band Monte Carlo perspective. *Appl. Phys. Lett.* **106**, 061112 (2015).
11. P. Kozodoy, J.P. Ibbetson, H. Marchand, P.T. Fini, S. Keller, J.S. Speck, S.P. DenBaars, and U.K. Mishra: Electrical characterization of GaN p-n junctions with and without threading dislocations. *Appl. Phys. Lett.* **73**, 975 (1998).
12. J.W.P. Hsu, M.J. Manfra, D.V. Lang, S. Richter, S.N.G. Chu, A.M. Sergent, R.N. Kleiman, L.N. Pfeiffer, and R.J. Molnar: Inhomogeneous spatial distribution of reverse bias leakage in GaN Schottky diodes. *Appl. Phys. Lett.* **78**, 1685 (2001).
13. J.W.P. Hsu, M.J. Manfra, S.N.G. Chu, C.H. Chen, L.N. Pfeiffer, and R.J. Molnar: Effect of growth stoichiometry on the electrical activity of screw dislocations in GaN films grown by molecular-beam epitaxy. *Appl. Phys. Lett.* **78**, 3980 (2001).
14. E.J. Miller, X.Z. Dang, and E.T. Yu: Gate leakage current mechanisms in AlGaN/GaN heterostructure field-effect transistors. *J. Appl. Phys.* **88**, 5951 (2000).
15. L. McCarthy, I. Smorchkova, H. Xing, P. Fini, S. Keller, J. Speck, S.P. DenBaars, M.J.W. Rodwell, and U.K. Mishra: Effect of threading dislocations on AlGaN/GaN heterojunction bipolar transistors. *Appl. Phys. Lett.* **78**, 2235 (2001).
16. S. Ganguly, J. Verma, Z. Hu, H.G. Xing, and D. Jena: Performance enhancement of InAlN/GaN HEMTs by KOH surface treatment. *Appl. Phys. Express* **7**, 034102 (2014).
17. S. Hafiz, F. Zhang, M. Monavarian, S. Okur, V. Avrutin, H. Morkoç, and U. Özgür: Estimation of carrier leakage in InGaN light emitting diodes from photocurrent measurements. In *Proceedings of the International Society of Optical Engineering*, Vol. **9003**; SPIE, Bellingham, WA, 2014; p. 90031R.
18. T. Yokoyama, Y. Kamimura, K. Edagawa, and I. Yonenaga: Local current conduction due to edge dislocations in deformed GaN studied by scanning spreading resistance microscopy. *Eur. Phys. J.: Appl. Phys.* **61**, 10102 (2013).
19. C.M. Drum: Intersecting faults on basal and prismatic planes in aluminium nitride. *Philos. Mag.* **11**, 313 (1965).
20. D.N. Zakharov, Z. Liliental-Weber, B. Wagner, Z.J. Reitmeier, E.A. Preble, and R.F. Davis: Structural TEM study of nonpolar *a*-plane gallium nitride grown on $(11\bar{2}0)$ 4*H*-SiC by organometallic vapor phase epitaxy. *Phys. Rev. B* **71**, 235334 (2005).
21. G. Ramírez-Flores, H. Navarro-Contreras, A. Lastras-Martínez, R.C. Powell, and J.E. Greene: Temperature-dependent optical band gap of the metastable zinc-blende structure -GaN. *Phys. Rev. B* **50**, 8433 (1994).
22. B. Monemar: Fundamental energy gap of GaN from photoluminescence excitation spectra. *Phys. Rev. B* **10**, 676 (1974).
23. Y.T. Rebane, Y.G. Shreter, and M. Albrecht: Stacking Faults as Quantum Wells for Excitons in Wurtzite GaN. *Phys. Status Solidi A* **164**, 141 (1997).
24. M. Albrecht, S. Christiansen, G. Salviati, C. Zanotti-Fregonara, Y.T. Rebane, Y.G. Shreter, M. Mayer, A. Pelzmann, M. Kamp, K.J. Ebeling, M.D. Bremser, R.F. Davis, and H.P. Strunk: Luminescence Related to Stacking Faults in Heterepitaxially Grown Wurtzite GaN. *MRS Online Proc. Libr.* **468**, 293 (1997).
25. Z. Bandić, T. McGill, and Z. Ikonić: Electronic structure of GaN stacking faults. *Phys. Rev. B* **56**, 3564 (1997).
26. I. Tischer, M. Feneberg, M. Schirra, H. Yacoub, R. Sauer, K. Thonke, T. Wunderer, F. Scholz, L. Dieterle, E. Müller, and D. Gerthsen: I 2 basal plane stacking fault in GaN: Origin of the 3.32 eV luminescence band. *Phys. Rev. B* **83**, 035314 (2011).
27. Y.J. Sun, O. Brandt, U. Jahn, T.Y. Liu, A. Trampert, S. Cronenberg, S. Dhar, and K.H. Ploog: Impact of nucleation conditions on the structural and optical properties of M-plane $GaN(1\bar{1}00)$ grown on $\gamma - LiAlO_2$. *J. Appl. Phys.* **92**, 5714 (2002).
28. B. Skromme, L. Chen, M. Mikhov, H. Yamane, M. Aoki, and F. DiSalvo: Properties of the 3.4 eV Luminescence Band in GaN and its Relation to Stacking Faults. *Mater. Sci. Forum* **457**, 1613 (2004).
29. R. Liu, A. Bell, F.A. Ponce, C.Q. Chen, J.W. Yang, and M.A. Khan: Luminescence from stacking faults in gallium nitride. *Appl. Phys. Lett.* **86**, 021908 (2005).
30. J. Lähnemann, O. Brandt, U. Jahn, C. Pfüller, C. Roder, P. Dogan, F. Grosse, A. Belabbes, F. Bechstedt, A. Trampert, and L. Geelhaar: Direct experimental determination of the spontaneous polarization of GaN. *Phys. Rev. B* **86**, 081302 (2012).

https://doi.org/10.1557/jmr.2015.273 Published online by Cambridge University Press

31. J. Lähnemann, U. Jahn, O. Brandt, T. Flissikowski, P. Dogan, and H.T. Grahn: Luminescence associated with stacking faults in GaN. *J. Phys. D: Appl. Phys.* **47**, 423001 (2014).
32. G. Jacopin, L. Rigutti, L. Largeau, F. Fortuna, F. Furtmayr, F.H. Julien, M. Eickhoff, and M. Tchernycheva: Optical properties of wurtzite/zinc-blende heterostructures in GaN nanowires. *J. Appl. Phys.* **110**, 064313 (2011).
33. J. Piprek and S. Nakamura: Physics of high-power InGaN/GaN lasers. *IEE Proc.: Optoelectron.* **4**, 145 (2002).
34. J.F. Van der Maelen Uría, S. García-Granda, and A. Menéndez-Velázquez: Solving one-dimensional Schrödinger-like equations using a numerical matrix method. *Am. J. Phys.* **64**, 327 (1996).
35. F. Scholz, S. Schwaiger, J. Däubler, I. Tischer, K. Thonke, S. Neugebauer, S. Metzner, F. Bertram, J. Christen, H. Lengner, J. Thalmair, and J. Zweck: Semipolar GaInN quantum well structures on large area substrates. *Phys. Status Solidi B* **249**, 464 (2012).
36. V. Darakchieva, B. Monemar, and A. Usui: On the lattice parameters of GaN. *Appl. Phys. Lett.* **91**, 031911 (2007).
37. W. Paszkowicz, S. Podsiadło, and R. Minikayev: Rietveld-refinement study of aluminium and gallium nitrides. *J. Alloys Compd.* **382**, 100 (2004). Proceedings of the European Materials Research Society Fall Meeting, Symposium B.
38. I. Vurgaftman and J.R. Meyer: Band parameters for nitrogen-containing semiconductors. *J. Appl. Phys.* **94**, 3675 (2003).
39. F. Bernardini, V. Fiorentini, and D. Vanderbilt: Spontaneous polarization and piezoelectric constants of III-V nitrides. *Phys. Rev. B* **56**, R10024 (1997).
40. M. Feneberg, K. Lange, C. Lidig, M. Wieneke, H. Witte, J. Bläsing, A. Dadgar, A. Krost, and R. Goldhahn: Anisotropic absorption and emission of bulk ($1\bar{1}00$) AlN. *Appl. Phys. Lett.* **103**, 232104 (2013).
41. L.C. de Carvalho, A. Schleife, and F. Bechstedt: Influence of exchange and correlation on structural and electronic properties of AlN, GaN, and InN. *Phys. Rev. B* **84**, 195105 (2011).
42. J.S. Im, A. Moritz, F. Steuber, V. Härle, F. Scholz, and A. Hangleiter: Radiative carrier lifetime, momentum matrix element, and hole effective mass in GaN. *Appl. Phys. Lett.* **70**, 631 (1997).
43. T. Azuhata, T. Sota, K. Suzuki, and S. Nakamura: Polarized Raman spectra in GaN. *J. Phys.: Condens. Matter* **7**, L129 (1995).
44. M. Feneberg, M.F. Romero, M. Röppischer, C. Cobet, N. Esser, B. Neuschl, K. Thonke, M. Bickermann, and R. Goldhahn: Anisotropic absorption and emission of bulk ($1\bar{1}00$) AlN. *Phys. Rev. B* **87**, 235209 (2013b).
45. B. Neuschl, J. Helbing, M. Knab, H. Lauer, M. Madel, K. Thonke, T. Meisch, K. Forghani, F. Scholz, and M. Feneberg: Composition dependent valence band order in c-oriented wurtzite AlGaN layers. *J. Appl. Phys.* **116**, 113506 (2014).
46. M. Feneberg, M. Röppischer, C. Cobet, N. Esser, J. Schörmann, T. Schupp, D.J. As, F. Hörich, J. Bläsing, A. Krost, and R. Goldhahn: Optical properties of cubic GaN from 1 to 20 eV. *Phys. Rev. B* **85**, 155207 (2012).
47. M. Röppischer, R. Goldhahn, G. Rossbach, P. Schley, C. Cobet, N. Esser, T. Schupp, K. Lischka, and D.J. As: Dielectric function of zinc-blende AlN from 1 to 20 eV: Band gap and van Hove singularities. *J. Appl. Phys.* **106**, 076104 (2009).
48. V. Bougrov, M.E. Levinshtein, S.L. Rumyantsev, and A. Zubrilov: *Properties of Advanced Semiconductor Materials: GaN, AlN, InN, BN, SiC, SiGe*; M.E. Levinshtein, S.L. Rumyantsev, and M. Shur eds.; John Wiley & Sons, New York, 2001.
49. T. Suzuki, H. Yaguchi, H. Okumura, Y. Ishida, and S. Yoshida: Optical Constants of Cubic GaN, AlN, and AlGaN Alloys. *Jpn. J. Appl. Phys.* **39**, L497 (2000).
50. T. Wunderer, J. Hertkorn, F. Lipski, P. Brückner, M. Feneberg, M. Schirra, K. Thonke, I. Knoke, E. Meissner, A. Chuvilin, U. Kaiser, and F. Scholz: Optimization of semipolar GaInN/GaN blue/green light emitting diode structures on {1-101} GaN side facets. *Proc. SPIE* **6894**, 68940V (2008).
51. M. Knab, M. Hocker, T. Felser, I. Tischer, J. Wang, F. Scholz, and K. Thonke: EBIC investigations on polar and semipolar InGaN LED structures. *Phys. Status Solidi B* (2015). doi: 10.1002/pssb.201552284.
52. I. Tischer, M. Feneberg, M. Schirra, H. Yacoub, R. Sauer, K. Thonke, T. Wunderer, F. Scholz, L. Dieterle, E. Müller, and D. Gerthsen: Stacking fault-related luminescence features in semi-polar GaN. *Phys. Status Solidi B* **248**, 611 (2011).
53. I. Tischer, M. Frey, M. Hocker, L. Jerg, M. Madel, B. Neuschl, K. Thonke, R. Leute, F. Scholz, H. Groiss, E. Müller, and D. Gerthsen: Basal plane stacking faults in semipolar AlGaN: Hints to Al redistribution. *Phys. Status Solidi B* **251**, 2321 (2014).
54. T. Narita, Y. Honda, M. Yamaguchi, and N. Sawaki: The surface diffusion of Ga species on an AlGaN facet structure in low pressure MOVPE. *Phys. Status Solidi C* **4**, 2506 (2007).
55. L. Vegard: Die Konstitution der Mischkristalle und die Raumfüllung der Atome. *Z. Phys.* **5**, 17 (1921).

https://doi.org/10.1557/jmr.2015.273 Published online by Cambridge University Press